CHALMERS

Spray Drying in Cyclone Separators

Thesis for the Degree of Master of Science in Chemical Engineering

Niklas Persson

Department of Chemical Engineering
Division of Chemical Reaction Engineering
Chalmers University of Technology
Gothenburg, Sweden 2014

Thesis for the Degree of Master of Science

Spray Drying in Cyclone Separators

Niklas Persson

Examiner:
Bengt Andersson
Supervisor:
Mohammad El-Alti

Department of Chemical Engineering
Chalmers University of Technology
Gothenburg, Sweden 2014

Spray Drying in Cyclone Separators

Niklas Persson

Department of Chemical Engineering
Chalmers University of Technology
SE-412 96 Göteborg
Sweden
Telephone + 46 (0)31-772 1000

Gothenburg, Sweden 2014

Abstract

A gas-solid cyclone separator is a separation device that separates solid particles from a gas phase by the use of a centrifugal force field. In traditional spray drying a cyclone separator is often included in a succeeding separation step, after a spray drying chamber. This thesis a study of whether spray drying in cyclone separators is possible. If the spray drying can be conducted in the cyclone, the spray drying chamber can be removed from process and the investment cost lowered.

The flow field in the studied cyclone was simulated in both two and three dimensions, with good agreement in the middle of the cyclone, where the region of interest is located. Single particle simulations, together with hand calculations and a factorial designed parameter study showed that spray drying is possible in the studied cyclone. However, for lower gas velocities than typical operational conditions and for droplets in the order of magnitude of a normalized diameter of 0.22 and smaller, where the droplet diameter is normalized against the largest droplets in the current system. By increasing the normalized cyclone diameter from 1.4 to 1.7, droplets up to the size of 0.5 can be dried before impinging the wall. The results were in compliance with experiments.

Acknowledgements

This thesis has been performed at ALTEN AB and Chalmers University of Technology in Göteborg, Sweden, during the period September to December 2013. The work has been supervised by Dr. Mohammad El-Alti at ALTEN AB, Professor Bengt Andersson and Assistant Professor Ronnie Andersson at Chalmers University of Technology.

I wish to acknowledge the help provided by my supervisors Dr. Mohammad El-Alti, Professor Bengt Andersson and Assistant Professor Ronnie Andersson for their help and guidance throughout the project.

Last but not least I would like to thank the members of the analysis and simulation group at ALTEN AB and my thesis colleague Erik Andersson.

Nomenclature

Acronyms

LES	Large Eddy Simulation
NS	Navier Stokes Equations
PVC	Precessing Vortex Core
RNG	Mathematical Renormalization-group technique
RSM	Reynolds Stress Model
UDF	User Defined Function]
RANS	Reynolds Decomposed and Averaged Navier Stokes Equations

Greek Symbols

α	Loading
δ	Dirac Delta
ϵ	Numerical Error
γ	Thermal conductivity $[W/mK]$
κ	Von Kármán Constant
λ	Surface Roughness [-]
$\mathcal{E}$	Dissipation of Turbulent Kinetic Energy $[J/kgs = m^2/kg^3]$
ν	Kinematic Viscosity $[m^2/s]$
ν_T	Turbulent Viscosity [Pas]
ρ	Density $[kg/m^3]$
σ	Surface Tension [N/m]
σ_k	Prandtl-Schmidt Number
τ	Characteristic Time [s]
τ_{ij}	Stress [Pa]
θ	Angle [°]

Roman Symbols

A_d	Projected Area $[m^2]$

C_D	Drag Coefficient [-]
C_p	Heat Capacity $[J/kgK]$
d	Dispersed Phase
$D_{i,m}$	Diffusivity Coefficient for Specie i $[m^2/s]$
F	Force [N]
h	Convective Heat Transfer Coefficient $[W/m^2K]$
h_{fg}	Heat of Evaporation $[J/kg]$
i, j, k	Direction
k	Turbulent Kinetic Energy, $[J/kg = m^2/s^2]$
k_c	Mass Transfer Coefficient $[m/s]$
M	Molality [mol/kg]
m	Mass [kg]
N	Flux $[Mol/m^2s]$
n	Mole
Nu	Nusselt Number [-]
P	Pressure [Pa]
p	Particle
P_0	Vapor Pressure [Pas]
Pr	Prandtl Number [-]
R	Universal Gas Constant [J/molK]
r	Radius [m]
Re	Reynolds Number [-]
Sc	Schmidt Number [-]
St	Stokes Number [-]
T	Temperature [K]
t	Time [s]
U	Velocity, [m/s]
u	Fluctuating Velocity $[m/s]$
V	Volume $[m^3]$
We	Weber Number [-]

X	Grid Spacing [m]
y^+	Dimensionless Distance [-]

Subscripts

∞	Bulk Conditions
f	Fluid
m	Molar
s	Surface
w	viscous, e.g viscous stress

Contents

1 Introduction

This chapter describes the background to the thesis, beginning with a description of traditional spray drying. Further on, the idea of spray drying in cyclones is introduced and the aim with the project is stated.

The process studied and some of the results in this thesis are classified. Therefore, the numerical values in this thesis are normalized.

1.1 Spray Drying

Spray drying is a method of drying a solution or a slurry, in order to produce a powder. This is done by dispersing the liquid into a gas phase. Major benefits of spray drying is that the particle size can be controlled by the atomization of the liquid, and spray drying is a fast process compared to other drying methods. The typical spray dryer consists of a spray drying chamber, where the spray is dried, and succeeding separation equipment such as one or more cyclone separators. When it comes to the atomization device it varies between applications, however, the two most common types are rotary disks and single fluid high pressure nozzles. An example of a nozzle is given in appendix G, which is also the nozzle used in the experimental part of this thesis.

The background for the thesis is a potential of reducing investment cost since the spray drying chamber is not needed, if it is possible to dry the liquid in the cyclone. Also the operational cost has a potential of being reduced.

1.2 Purpose

The purpose for this thesis is to investigate whether spray drying is possible in cyclone separators, and can be seen as a feasibility study. There will be a fundamental description of the droplet behavior in the cyclone and correlations to problems in conventional spray drying when it comes to sticking of the discrete phase on the wall. A parameter study will be conducted in order to determine the influence on the drying efficiency of several factors, with the approach of avoiding wet particle impact on the cyclone wall. This approach was chosen since one of the major problems in traditional spray drying is sticking of the discrete phase on the wall.

As complement to the theoretical study and simulations, experimental investigation was conducted, which can be seen as both complement to the theoretical study and as confirmation of results obtained from simulations and hand calculations.

The aim of the thesis is not to derive a concept for successful spray drying in cyclones, but rather to investigate the possibility and point out the direction for future work.

1.3 Constraints

The focus of the thesis is to describe single droplet behavior, both in the gas phase and at wall impact. Due to limited computational recourses focus of the simulations will be in 2D, with verification in 3D. Since focus was on single droplet behavior, no simulations of a liquid spray with collision and breakup of droplets was conducted.

2 Theory

The theory section starts with a description of a typical gas solid reverse flow cyclone, which is given in section 2.1. Section 2.2 describes the fundamentals of CFD and also the modeling of turbulence and the choice of turbulence model. In section 2.3 the modeling of the discrete phase is described, and finally section 2.4 describes the heat and mass transfer from the droplet.

2.1 The Reversed-Flow Cyclone

In figure 2.1 below, the different parts of the cyclone is pointed out.

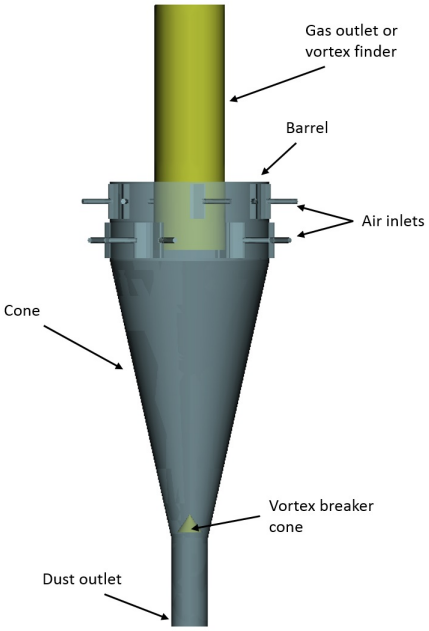

Figure 2.1: The different parts of the studied cyclone

The tangential gas inlets induce a strong swirling flow, moving downwards in the cyclone. The downward motion of the this vortex is reversed at the bottom of the cyclone, and the gas flow is thus moving upwards forming an inner vortex, and exists through the gas outlet at the top of the cyclone. For the inner part of the outer vortex the tangential velocity can be described as a rigid body rotation with increasing velocity in the radial direction, whilst the outer region has a decreasing tangential velocity limited by the wall boundary layer. Further on, the strong swirling flow is affecting the pressure profile in the cyclone, the maximum static pressure is found at the outer walls and decreasing towards the axis of the cyclone, where the static pressure may fall below atmospheric pressure. In addition the flow field in the cyclone exhibits low frequency

oscillations, where the formed vortex moves in three dimensions with a time dependence. This phenomenon is known as *precessing vortex core* (PVC) [12].

Due to the swirling flow of the gas, the particles are subjected to a strong centrifugal force field, and the effect of the particles inertia is that they are transported radially towards the wall. At the wall, the particles will be transported to the dust outlet due to the motion of the boundary layer and gravitational force [12]. The particle size is important in the separation, too small particles will exit with the gas whilst the larger particles exit through the dust outlet.

2.2 Modeling the Flow Field

In *computational fluid dynamics* the governing equations for continuity, momentum, energy and species are solved. Generally there are no analytical solutions, so the equations must be solved numerically [1]. Upon solving PDEs with numerical methods an error is introduced, and it is important to bear in mind that the error will always exist for numerical solutions. The error is depending upon the step size, which in the CFD case is equivalent to the size of the computational cells, and will thus decrease with a denser mesh. However, depending on the discretization scheme used, the order of the accuracy differs and gives information on how fast the error decreases when reducing the step size. For an n^{th} order accurate discretization scheme, the error is proportional to the n^{th} power of the grid spacing, $\epsilon = C\Delta X^n$. However, low order accuracy schemes tends to be more stable than higher, so there might be an trade off between grid density and discretization scheme.

2.2.1 Modeling Turbulence

The Navier Stokes equation (equation 2.1) describes motion of fluids, and is obtained by applying Newtons second law to fluid motion [10].

$$\frac{\partial U_i}{\partial t} + U_j \frac{\partial U_i}{\partial x_j} = -\frac{1}{\rho}\frac{\partial P}{\partial x_i} + \nu \frac{\partial^2 U_i}{\partial x_j \partial x_j} \tag{2.1}$$

Where U is the velocity, ρ is the density and P is the pressure. The Navier-Stokes equations describes turbulent flow, however, it is in most situations not possible to solve the equations direct due to the small spatial and time-scales needed in order to resolve the smallest turbulent scales. In order to describe the turbulence some degree of modeling is needed, and depending on the complexity of the flow and computational recourses at hand the degree of modeling varies. Either can the largest turbulent eddies be resolved and the smaller scales modeled, by Large Eddie Simulation, or the turbulent fluctuation may not be possible to resolve at all. The latter is the most common in engineering problems and the turbulence is modeled by Reynolds decomposition and averaging of the Navier-Stokes equations (RANS). Even though the turbulent fluctuations are averaged, reasonable velocity averages can be obtained by the RANS models. A consequence of the modeling is that properties of the flow at scales smaller than the grid is not resolved, e.g. mixing of species, and additional models needs to be included in order to describe these phenomena [1].

By Reynolds averaging and decomposition of the pressure and velocity in equation 2.1, into a mean part and a fluctuating part, $U_i = \langle U_i \rangle + u_i$ and $P = \langle P \rangle + p$, the flow can be described by the mean flow and turbulence quantities. By time-averaging over a reasonable time, and substitution

in equation 2.1, the Reynolds Averaged Navier Stokes (RANS) equations are obtained. Noting that the average of linear fluctuating terms equals zero, the RANS can be stated as equation

$$\frac{\partial \langle U_i \rangle}{\partial t} + \langle U_j \rangle \frac{\partial \langle U_i \rangle}{\partial x_j} = -\frac{1}{\rho}\frac{\partial \langle P \rangle}{\partial x_i} + \nu \frac{\partial^2 \langle U_i \rangle}{\partial x_j^2} - \frac{\partial \langle u_i u_j \rangle}{\partial x_j} \tag{2.2}$$

As can be seen the equation is very similar to the original Navier-Stokes equation (2.1), the introduced term $-\rho\langle u_i u_j \rangle$ is referred to as the Reynolds stress, and is important because of the coupling between the mean and fluctuating parts. The Reynolds stress term must be modeled in order to close equation 2.2. Since the Reynolds stresses are unknown, some assumptions has to be made. The Boussinesq approximation is a simple approximation based on the assumption that the components of the Reynolds stresses are proportional to the gradients of the mean velocity. The approximation proposes that the turbulent transport of momentum is a diffusive process, and analogous to molecular viscosity modeled by a turbulent viscosity. The Boussinesq approximation is defined in equation 2.3 below,

$$\frac{\tau_{ij}}{\rho} = -\langle u_i u_j \rangle = \nu_T \left(\frac{\partial \langle U_i \rangle}{\partial x_j} + \frac{\partial \langle U_j \rangle}{\partial x_i} \right) - \frac{2}{3} k \delta_{ij} \tag{2.3}$$

Where the introduced term, k, is the turbulent kinetic energy per unit mass and defined as, $k = 1/2\langle u_i u_i \rangle$. The Boussinesq approximation comes with some limitation, and the analogy to molecular diffusivity proposes that the turbulence is isotropic, and also that there is an equilibrium between stress and strain. However, the Boussinesq approximation is widely used and a cornerstone in several turbulence models. The main reason is the reduction in computational cost compared to the use of higher order closure models. In order to solve the unknown turbulent kinetic energy, a transport equation for k is introduced, equation 2.4,

$$\underbrace{\frac{\partial k}{\partial t}}_{1} + \underbrace{\langle U_j \rangle \frac{\partial k}{\partial x_j}}_{2} = -\underbrace{\langle u_i u_j \rangle \frac{\langle \partial U_i \rangle}{\partial x_j}}_{3} - \underbrace{\nu \left\langle \frac{\partial u_i}{\partial x_j} \frac{\partial u_j}{\partial x_i} \right\rangle}_{4} + \frac{\partial}{\partial x_j} \left(\underbrace{\nu \frac{\partial k}{\partial x_j}}_{5} - \underbrace{\frac{\langle u_i u_i u_j \rangle}{2}}_{6} + \underbrace{\frac{\langle u_j p \rangle}{\rho}}_{7} \right) \tag{2.4}$$

where the different terms are

1. Accumulation of turbulent kinetic energy.
2. Convective transport of turbulent kinetic energy by the mean flow.
3. Production of turbulent kinetic energy, large eddies extract energy from the mean field.
4. Dissipation of turbulent kinetic energy by viscous stress.
5. Molecular diffusion of turbulent kinetic energy.
6. Transport of kinetic energy due to velocity fluctuations.
7. Transport of kinetic energy due to pressure fluctuations.

In equation 2.4 the terms 3, 4, 6 and 7 are unknown, implying the need of assumptions. Term 3 is modeled with the previous described Boussinesq approximation, term 6 and 7 is modeled assuming a gradient-diffusion transport mechanism. The closure of term 4, dissipation of

turbulent kinetic energy is achieved by defining the dissipation of turbulent kinetic energy as, $\mathcal{E} = \nu\langle\frac{\partial u_i}{\partial x_j}\frac{\partial u_i}{\partial x_j}\rangle$, and deriving a transport equation for $\mathcal{E}$, in similar manner as for the k-equation. The transport equation for $\mathcal{E}$, with closures, is defined in equation 2.5 below,

$$\underbrace{\frac{\partial \mathcal{E}}{\partial t}}_{1} + \underbrace{\langle U_j\rangle\frac{\partial \mathcal{E}}{\partial x_j}}_{2} - \underbrace{C_{\mathcal{E}1}\nu_T\frac{k}{\mathcal{E}}\left[\left(\frac{\partial\langle U_i\rangle}{\partial x_j} + \frac{\partial\langle U_j\rangle}{\partial x_i}\right)\frac{\partial\langle U_i\rangle}{\partial x_j}\right]}_{3} - \underbrace{C_{\mathcal{E}2}\frac{\mathcal{E}^2}{k}}_{4} + \underbrace{\frac{\partial}{\partial x_j}\left[\left(\nu + \frac{\nu_T}{\sigma_k}\right)\frac{\partial \mathcal{E}}{\partial x_j}\right]}_{5} \tag{2.5}$$

where the different terms are

1. Accumulation of dissipation.
2. Convective transport of dissipation by the mean flow.
3. Production of $\mathcal{E}$.
4. Dissipation of $\mathcal{E}$.
5. Diffusion of $\mathcal{E}$.

and $C_{\mathcal{E}1,2}$ are model coefficents.

By introducing two new quantities, k and $\mathcal{E}$, with corresponding transport equations, the RANS equations can be closed. The model is called the Standard $k-\mathcal{E}$ model and is one of the most used turbulence models.

Choice of Turbulence Model

The standard $k-\mathcal{E}$ model is however not suited to model the flow in the cyclone, it will be too dissipative. At high strain rates the turbulent viscosity tends to be too high, resulting in dampening of vortices. The underlying problem is the Boussinesq hypothesis, which imposes isotropy, and the way the dissipation equation is modeled. An improved model for handling swirling flows is the RNG $k-\mathcal{E}$ model, in which an additional term in the transport equation for $\mathcal{E}$ is added, resulting in smaller destruction of $\mathcal{E}$ at high strain rates [1]. By using a mathematical renormalization-group (RNG) technique, the Navier-Stokes equations can be renormalized to account for the smaller scales of motion. In contrast the standard $k-\mathcal{E}$ model, in which the eddy viscosity is determined from a single turbulence length scale, the RNG-model attempts to account for the different scales of motion, since in reality all scales of motion will contribute to turbulent diffusion [13]. The result is the modified form of the $\mathcal{E}$-equation with the extra production term, to be added on the right hand side of equation 2.5, which is defined in equation 2.6. The effective viscosity will be reduced, and thus the dampening of vortices and the additional term is,

$$S_{\mathcal{E}} = -2\nu S_{ij}\langle\frac{\partial u_l}{\partial x_i}\frac{\partial u_l}{\partial x_j}\rangle \tag{2.6}$$

and modeled as

$$S_{\mathcal{E}} = \frac{c_\mu\eta^3\left(1-\eta/\eta_0\right)\mathcal{E}^2}{\left(1+\beta\eta^3\right)k} \tag{2.7}$$

where $\eta = \frac{k}{\mathcal{E}}\sqrt{2S_{ij}S_{ij}}$ and S_{ij} is the strain-rate tensor.

According to Meier and Mori [14], who has simulated the gas flow field in a cyclone in two dimensions, only anisotropic turbulence models can predict the swirling gas flow in a cyclone with satisfactory results. However, in their study the comparison was only between the isotropic standard $k-\mathcal{E}$ model and an anisotropic model composed of a combination of the standard $k-\mathcal{E}$ model and the mixing length model of Prandtl. Even though the conclusions from Meier and Mori is consistent with previous stated unsuitability of the standard $k-\mathcal{E}$ model, it does not tell whether the RNG $k-\mathcal{E}$ model could predict the flow. Although the statement of Meier and Mori opposes the use of RNG $k-\mathcal{E}$ model, which is an isotropic turbulence model, the comparison included only the standard $k-\mathcal{E}$ model for as representative of isotropic turbulence models.

Hoekstra et al. [15] have reported reasonable agreement with experimental data of gas flow in a cyclone using Reynolds stress models (RSM), in which transport equations for the Reynolds stresses are used for closing the Navier-Stokes equations, equaton 2.1 [1]. By the use of transport equations for the Reynolds stresses, a major drawback with the $k-\mathcal{E}$-based models, the Boussinesq approximation, is removed and the model is of higher fundamental level [1]. However, the price comes with higher computational costs. G. Gronald et. al [16] points out the importance of noting that the above results is not only based on average velocities, but also velocity fluctuations. The importance can be depicted by thinking of the separation process in a cyclone as a competition between the centrifugal force acting on the particle towards the periphery, and the turbulent diffusivity thats spreads the dispersed phase in the domain. The effect of the fluctuations is increasing the chance of the particles to enter the gas stream leaving the cyclone, instead of exiting through the dust outlet.

Further on, Gronald [16] reports problem with a steady state RANS approach to predict the flow field, which most probable explanation is the phenomena of precessing vortex core (PVC), i.e. there is no steady-state solution. In laser doppler anemometry measurements used for validation of Gronalds simulations, the PVC was confirmed [16]. In order to deal with the unsteady-state condition due to the PVC, Gronald brought the simulations to a quasi-steady state from which a transient simulation proceeded, and the properties of interest was time-averaged [16]. The most important conclusion from Gronald et. al. is that the RSM provides industrially relevant results with limited computational cost, compared with LES.

The scope of this thesis is neither to predict the flow field in the cyclone with high accuracy, nor a detailed capture of the classification of particles, but rather on a quantitative level investigate possibilities of spray drying i cyclone separators. Even though the RNG $k-\mathcal{E}$ model describes the flow field inferior to RSM and LES, the model shows improved prediction compared to standard $k-\mathcal{E}$ [15]. The RNG $k-\mathcal{E}$ model will be used for modeling turbulence in this Thesis.

2.2.2 Near Wall Modeling

In the vicinity of the wall rapid changes of flow variables occurs, from the turbulent bulk flow to zero velocity at the wall. Close to the wall, where the viscous forces are large, turbulence models like the RNG $k-\mathcal{E}$ model are not valid. There are basically two approaches to handle the near wall region, the first approach is to use a modified turbulence model which can account for the dominant viscous forces, and resolve the flow field. This implies a very fine mesh due to the rapid change of flow variables. The second approach is to model the near wall region, instead of resolving it, to obtain boundary conditions for the turbulence model [1].

For resolving the flow field at the wall, the first grid point of the mesh should be at a $y^+ < 5$, where y^+ is a dimensionless distance from the wall, defined in equation 2.8 below.

$$y^+ = \frac{y}{l_*} \tag{2.8}$$

The dimensionless length, y^+, is based upon a characteristic velocity and length scale for the viscous sublayer. The characteristic velocity scale is defined as $u_* = \sqrt{\tau_w/\rho}$, where ρ is the density and τ_w is the viscous stress. The characteristic length scale is defined as $l_* = v/u_*$.

For the second approach, modeling the flow field in the near wall region, the standard wall function is commonly used. The standard wall function is based upon assumptions that the flow is parallel to the wall, that there is a constant stress layer in the inner sublayer, where the sum of viscous stresses and Reynolds stresses are constant. The near wall region is then modeled by the *logarithmic law of the wall*, defined in equation 2.9 [1].

$$\langle U_x \rangle^+ = \frac{1}{\kappa} \ln(y^+) + B \tag{2.9}$$

Where κ and B are constants and the x-velocity is the velocity component parallel to the wall. A major drawback with the wall function approach is that the numerical result is adverse affected by a fine grid in the near wall region. y^+-values below 15 gradually results in unbound errors [3], it is recommended to have a first grid point above $y+ = 20 - 30$ but not larger than 100 [1].

The wall function approach comes with limitations. When the assumptions stated for the standard wall function is not valid, e.g for flow separation or impinging flow, a non-equilibrium wall function can be used, which applies a two zonal layer concept. The law of the wall for mean temperature and species remains the same, however, the effect of pressure gradients in the logarithmic law of the wall is included for mean velocity. Even though the non-equilibrium wall function performs better than the standard for complex flows, the results are still affected by severe pressure gradients and high three-dimensionality in the near wall region [3].

Enhanced wall treatment [3] is a method for near wall modeling that combines the two layer model with so called enhanced wall functions. If the first grid point is at $y^+ \approx 1$, the flow is resolved, whilst for larger y^+ values the near wall region is modeled. In order to handle even the intermediate range, $3 < y^+ < 10$, the logarithmic law of the wall is blended with a linear laminar law of the wall [3].

2.3 Modeling the Discrete Phase

In this section the force balance for the particles is stated together with the characterization of the multiphase flow. The theory behind the events of wall impact are stated. Further on, the vapor pressure for the discrete phase and the correlations for heat and mass transfer are described.

2.3.1 Forces acting on the particles

Following is a description of potential forces acting on the discrete phase, and whether to be included or not in the force balance on the particle.

Drag force

The drag force is a function of the relative velocity and the cross sectional area of the particle, the drag force is included in the simulation and is calculated according to equation 2.10,

$$F_{drag} = \frac{1}{2} A_d C_D \rho_f |U_{i,f} - U_{i,d}| \left(U_{i,f} - U_{i,d}\right) \tag{2.10}$$

where A_d is the projected area, C_D is the drag coefficient and is in Ansys Fluent calculated according to Morsi et. al [2] with equation 2.11 below,

$$C_D = a_1 + \frac{a_2}{Re_d} + \frac{a_3}{Re_d} \tag{2.11}$$

where a_1, a_2 and a_3 are constants for a given Reynolds regime. If the particle Mach number is higher than 0.4 or the particle Reynolds number is higher than 20, additional corrections is added to equation 2.11. A somewhat simplified model for calculating the drag coefficient is equation 2.12.

$$C_D = \begin{cases} \dfrac{24}{Re_d} & \text{if } Re_d < 0.5 \\ \dfrac{24}{Re_d}\left(1 + 0.15 Re_d^{0.687}\right) & \text{if } 0.5 < Re_d < 1000 \\ 0.44\alpha_d & \text{if } Re_d > 1000 \end{cases} \tag{2.12}$$

Here is α the loading of the dispersed phase. Important to note is that the above equations are describing solid particles. For fluid particles at low particle Reynolds number the drag is generally lower due to internal circulation. Whereas for high Weber number the shape of the droplet is distorted, and approaches a disk-shape at high enough Weber number.

Buoyancy force and gravitational force

The buoyancy force is a result of the density difference between the dispersed phase and the continuous phase. In this case the continuous phase density is much smaller than the discrete phase density, therefore the buoyancy force can be neglected and is not included in the force balance 2.13. The gravitational acceleration is included in the simulations.

Turbulent forces

Turbulent forces are acting on a particle in a turbulent flow field. The force is modeled as a random addition to the fluid phase velocity, sustained for the minimum of either the lifetime of an eddy or the time it takes for the particle to pass through an eddy. Turbulent forces are included in the simulations of the discrete phase.

Forces not to be included

The fluid close to the particle is accelerated when there is a velocity difference between the phases, and there is an added *virtual mass* to the particle. This is the virtual mass force. If the continuous phase density is much lower than the discrete phase density the effect of the virtual mass force can be neglected, as in this case.

Other forces not included in the simulations are the Magnus and Saffman lift forces, which is the result of rotating particle or velocity gradients over the particle. The history force accounts for the time taken for the boundary layer to equilibrate to new conditions, and is not included. Since

the particles are large compared to molecules, the Brownian motion is not included, neither is the thermophoretic force.

Force balance

Generally the force balance on the particle can be expressed according to Newtons second law, as in equation 2.13 below.

$$m_d \frac{dU_{i,d}}{dt} = \sum_{i=1}^{n} F_n \tag{2.13}$$

Here F represents the different forces on the particle and including only the relevant forces, equation 2.13 can be expanded to equation 2.14.

$$m_d \frac{dU_{i,d}}{dt} = \frac{1}{2} A_d C_D \rho_f \left(U_{i,f} - U_{i,d}\right)^2 \tag{2.14}$$

2.3.2 Characterization of the Multiphase Flow

Stokes number corresponds to the behavior of a dispersed particle in a fluid flow and is defined as a characteristic time of the particle to a characteristic time of the fluid flow [1], according to equation 2.15 below,

$$St = \frac{\tau_d}{\tau_f} \tag{2.15}$$

where τ_d is the characteristic time for the discrete phase and τ_f the characteristic time for the fluid phase, e.g. the turbulence. The time for the particle in order to respond in changes of the continuous flow, the characteristic time for the particle, can be derived from equation 2.14. For simplicity the drag coefficient is assumed constant during the derivation of the response time, and so is also the continuous phase velocity. The response time can be defined as the time it takes for the particle to reach 63% of the continuous phase velocity. The derivation starts by differentiating and integrating equation 2.14.

$$\int_{U_{i,d,0}}^{0.63U_{i,f}} m_d \frac{dU_{i,d}}{dt} = \int_0^t \frac{1}{2} A_d C_D \rho_f \left(U_{i,f} - U_{i,d}\right)^2 dt \tag{2.16}$$

Assuming that no heat and mass transfer occurs during the velocity change, and for simplicity that the drag coefficient is constant equation 2.16 can be simplified accordingly,

$$\int_{U_{i,d,0}}^{0.63U_{i,f}} \frac{dU_{i,d}}{\left(U_{i,f} - U_{i,d}\right)^2} = \frac{1}{2} \frac{A_d C_D \rho_f}{m_d} \int_0^t dt \tag{2.17}$$

integrating equation 2.17 results in

$$\left[\frac{1}{\left(U_{i,f} - U_{i,d}\right)}\right]_{U_{i,d,0}}^{0.63U_{i,f}} = \frac{1}{2} \frac{A_d C_D \rho_f}{m_d} \Big[t\Big]_0^t \tag{2.18}$$

Simplifying equation 2.18 and the characteristic time for the particle can be calculated according to equation 2.19.

$$\tau_d = \frac{2m_d\left(\frac{1}{0.37u_{i,f}} - \frac{1}{u_{i,f-u_{i,d,0}}}\right)}{A_d C_D \rho_f} \tag{2.19}$$

The characteristic time for the fluid flow, τ_f, can be estimated from a characteristic length, l_s and characteristic velocity U_S as $\tau_s = l_s/U_s$. The larger scales of velocity for the fluid phase can be estimated with the geometry as constraint, whilst the velocity scale for the larger turbulence eddies can be estimated with equation 2.20.

$$U = \sqrt{\frac{2k}{3}} \tag{2.20}$$

2.3.3 Droplet wall interaction

When the droplet collides with a wall there are several possible outcomes. The behavior of the droplet after the wall impact is depending on both the characteristics for the droplet, as velocity and size, and on the properties of the wall, such as wall temperature. The maximum operating temperature for the studied cyclone is below the boiling point for the solution, the correlations presented in this section is valid in the region up to the boiling point of the solution. The droplet can either stick to the wall, rebound, spread or splash. In order to analyze the behavior of the impact the Weber number is a key parameter. The Weber number for a droplet is defined in equation 2.21 below.

$$We = \frac{\rho_d U_n^2 d}{\sigma} \tag{2.21}$$

Where ρ_d is the density of the discrete phase, U_n the normal velocity, d the droplet diameter and σ is the surface tension. The Weber number can be seen as the ratio of inertia to surface tension.

Following is a classification of events of single droplet-wall interaction. An overview of the impact regimes is given in figure 2.2, note that the region well covers the possible operational conditions for the relevant cyclone. The events are different for impact on a dry wall and a wall with a wall film, even though the same regions exists. The cases are presented separately in table 2.1 and 2.2 respectively.

Table 2.1: Droplet impact on dry wall, temperatures up to the boiling point

Boundary	Criterion	Comments
Stick/rebound	$We << 1$	
Rebound/spread	$We/(Re)^{0.5} = \frac{3}{4}(1 - cos(\theta))$	θ is the angle of impact [5]
Spread/splash	$We^{0.8}Re^{0.4} = 649 + 3.76\lambda_{nd}^{-0.63}$	$1.5e-5 < \lambda_{nd} < 0.86$, $\lambda_{nd} = \bar{\lambda}/d$ [6]

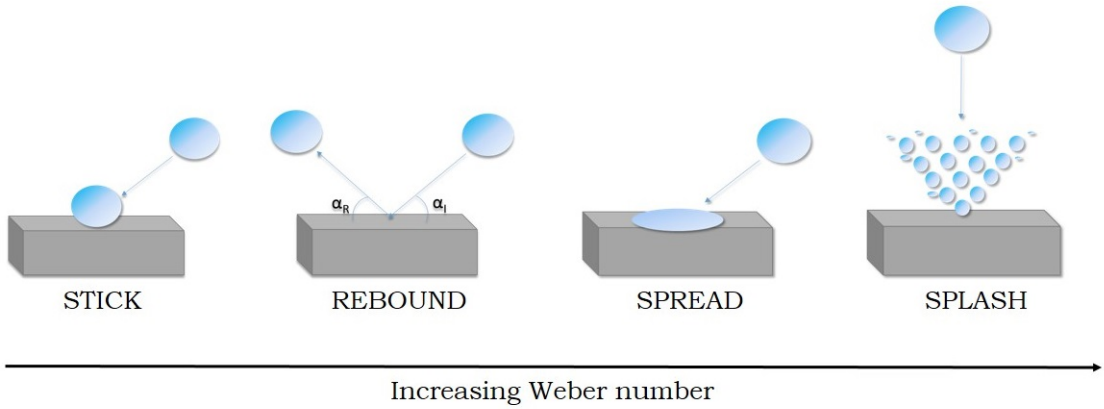

Figure 2.2: Overview of impacts regimes for single droplets on dry wall, valid for temperatures up to the boiling point of the liquid, reproduced from Bai and Gosman 1995 [20].

Table 2.2: Droplet impact on wet-wall, temperatures up to the boiling point

Boundary	Criterion	Comments
Stick/rebound	$We < 5$	[7]
Rebound/spread	$5 < We < 10$	Based on deep liquid layer and droplet diameter of 2.8 mm [7]
	$We \approx 20$	Neighboring effects by droplets considered [8]
Spread/splash	$We = 10^2 d(\rho_l/\sigma)^{1/2}\nu^{1/4}f^{3/4}$, $f = V_n/d$	$70 < d < 340\mu m$ [7] [9]

2.3.4 Vapor Pressure

Upon solving the heat and mass transfer for the evaporating droplet it is crucial to define the vapor pressure properly. The vapor pressure of pure water as a function of temperature can be expressed by the Antoine equation:

$$log_{10}P_0 = \left(1076 - \frac{230700}{T + 506.15}\right) \tag{2.22}$$

Where P is the pressure in Pa and T the temperature in Kelvin. Equation 2.22 is valid in the temperature range $274K < T < 373K$. The presence of sodium chloride in the water will lower the vapor pressure above the surface, and an empirical formula for the fractional lowering of vapor pressure can be expressed as equation 2.23 [4].

$$K = \frac{P_0 - P}{P_0 M} = \frac{\Delta P}{P_0 M} \tag{2.23}$$

where K for solutions at higher molality than 3 is

$$K = (M - 3)(0.0019772 - 0.00001193(T - 273.15)) + 0.035 \tag{2.24}$$

where M is the molality.

The vapor pressure is also affected by the curvature of the droplets, were small droplets, with high curvature, have higher vapor pressure. The Kelvin equation, 2.25, can be used to calculate the vapor pressure above a curved surface,

$$ln\frac{P}{P_0} = \frac{2\sigma V_m}{rRT} \tag{2.25}$$

where P is the actual vapor pressure, P_0 is the saturated vapor pressure without curvature effect, V_m, is the molar volume of the liquid, R is the universal gas constant, r the radius of the droplet and T the temperature in Kelvin. According to calculations in appendix B the effect of droplet curvature on the vapor pressure at room temperature is less than 3%. The surface tension decreases with temperature so the effect will be even lower at the operating conditions. Important to note is that the effect will be larger for smaller droplets and smaller for larger droplets. The effect of curvature is neglected in the simulations.

The resulting equation for the vapor pressure above the surface of the droplet is equation 2.26 below.

$$P = 10^{\left(1076 - \frac{230700}{T+233}\right)} \left(1 - ((M - 3)(0.0019772 - 0.00001193T) + 0.035)M\right) \tag{2.26}$$

2.4 Heat and Mass Transfer

In this section, the correlations for the heat and mass transfer to, and from, the particles are stated. These correlations are also the ones used in ANSYS Fluent.

2.4.1 Mass Transfer

The droplet will not reach the boiling point in the cyclone due to the normalized maximum inlet gas temperature of 1. Since the droplet will evaporate at a relatively low temperature, the vaporization can be described with a gradient diffusion approach where the flux of liquid from the droplet is related to the difference in vapor pressure at the surface and in the bulk gas phase [10]. The flux of specie i can be modeled with equation 2.27,

$$N_i = k_c \left(C_{i,s} - C_{i,\infty}\right) \tag{2.27}$$

where N_i is the molar flux, k_c is the mass transfer coefficient, $C_{i,s}$ is the surface concentration and $C_{i,\infty}$ is the bulk gas concentration. Using the ideal gas law, $PV = nRT$, it can be seen that the concentration is directly correlated to the partial pressure, by rearrangement,

$$\frac{n}{V} = C = \frac{P}{RT} \tag{2.28}$$

The mass transfer coefficient is calculated with the Fröessling equation, equation 2.29,

$$Sh_{AB} = \frac{k_c d_p}{D_{i,m}} = 2 + 0.552 Re_d^{1/2} Sc^{1/3} \tag{2.29}$$

where $D_{i,m}$ is the diffusivity coefficient for specie i in the gas phase and Sc is the Schmidt number, $Sc = \nu \rho D_{i,m}$ [23] [3].

2.4.2 Heat Transfer

The heat balance for the droplet is written in equation 2.30, and takes both convective heat transfer and the latent heat transfer in consideration,

$$m_p c_p \frac{dT_p}{dt} = hA_p(T_\infty - T_p) - \frac{dm_p}{dt} h_{fg} \tag{2.30}$$

where c_p is the droplet heat capacity, h is the convective heat transfer coefficient, h_{fg} is the heat of evaporation. The convective heat transfer coefficient is calculated with equation 2.31 [25],

$$Nu = \frac{hd_p}{\gamma_\infty} = 2 + 0.6 Re_d^{1/2} Pr^{1/3} \tag{2.31}$$

where Pr is the Prandtl number and γ_∞ is the conductivity of the gas phase.

3 Method

In this chapter the approach for how the simulations and calculations where performed is stated together with motivations.

3.1 Solving the Flow Field

In an early stage of the simulations, 2D simulations were performed on a smaller cyclone than the one presented in figure 2.1, which in addition had a cross mounted inside the vortex finder. In order to model the cross in 2D-simulations a zero swirl zone was specified inside the vortex finder, which is a similar approach to previous work [26]. From the results of the parameter study it could be seen that a larger diameter was beneficial, and a larger cyclone without the vortex finder cross was available for experiments. The 3D simulations was performed on this cyclone, and thus without the vortex finder cross, in contradiction to the 2D simulations.

As can be seen in figure 2.1 there are two levels of gas inlets, of which the lower section is slightly tilted upwards. Using both levels of gas inlets results in a longer particle-residence time and accumulation in the barrel. Initial simulations showed that by using only the upper level of gas inlets this time could be reduced significantly and because of this were only the upper level of gas inlets used throughout the simulations.

3.1.1 Boundary Conditions

The geometry was simplified for the 2D simulations, and an axis-symmetric boundary condition was used, meaning that the 2D-geometry is rotational symmetric around the axis. Further on, the gas inlets were represented as a gas inlet with defined velocity, the dust outlet and gas outlet were represented by two pressure outlets, where the boundary pressure was set to atmospheric. The no slip condition was used throughout the simulations. For the 3D simulations the same pressure outlet was defined on dust- and gas outlet, whereas for the inlets a pressure was defined in contrast to a defined velocity for the 2D case. The gas inlet velocity for the 2D simulations was calculated from the referens case, according to appendix A.

3.1.2 Solution Procedure

The solution was initialized with the hybrid initialization scheme. The scheme is a collection of different methods in order to produce an enhanced velocity profile for complex geometries, and a pressure field that smoothly connects high and low pressure values or boundaries. Variables like temperature and species are averaged, or calculated from a predetermined procedure [3].

All simulations were performed with the pressure-based coupled solver in Fluent. Unlike the segregated solver, the coupled solver solves the momentum and continuity equations in a single step. The result is a faster converging solution with the price of increased memory demand, since more information needs to be stored during each iteration [3]. Using the pressure-based coupled

solver it is possible to solve the steady-state problem with an pseudo-transient approach, which can be described as a form of implicit under-relaxation [17]. The under-relaxation is controlled by a pseudo time-step, which can either be the same, or different, for the different equations [3]. An overview for the settings used are presented in table 3.1

Table 3.1: Overview of simulation settings

Software	Fluent 14.5.0
Turbulence model	RNG $k-\mathcal{E}$
Gas flow	Compressible
Discretization scheme	Second order upwind
Pressure interpolation scheme	PRESTO!
Solver	Coupled

3.1.3 Judging Convergence

When it comes to judging the convergence, residuals and integral quantities where monitored. Area weighted averaged on several planes for temperature, velocity components and static pressure was monitored in addition to a total mass balance over the system. By using both an overall higher grid density and locally refined mesh the solutions grid-dependence was investigated, and judged negligible.

The second order upwind scheme was used throughout the simulations and in order to verify the accuracy, simulations with a third order discretization scheme was conducted. Also for the pressure-velocity coupling and pressure interpolation scheme, different alternatives were used and the combination giving the most stable results are presented in table 3.1.

From a converged solution the RNG $k-\mathcal{E}$ turbulence model was changed to realizable $k-\mathcal{E}$, in order to see the effects of changing model. Realizable $k-\mathcal{E}$ was not as stable as the RNG $k-\mathcal{E}$, and had higher residuals and integral quantities changing over iterations significantly more than for the RNG $k-\mathcal{E}$. However, the results, even though not converged, was in the same order of magnitude as those from the RNG $k-\mathcal{E}$. In order to ensure that the previous solution had no effect on the results from the realizable $k-\mathcal{E}$ simulation, simulations from a initialized conditions was conducted with the same results.

3.2 Discrete Phase

The forces and characterization of the multiphase flow, from section 2.3, was used to set up the simulations. In addition a reasoning of how the drying process most likely looks like is described in section 3.2.1 below. The heat of vaporization for the water in the droplets was set to a fixed value, since dependence was low, according to figure 4.6(b).

The model for the vapor pressure, equation 2.26, was implemented in a *User Defined Function* which was called upon in each iteration of the discrete phase simulations in Fluent.

3.2.1 Drying of Droplets

Depending on the characteristics of the solute, the crystallization can either start at the surface of the droplet and form a shell, or throughout the droplet. In the former case, when a shell is forming, the evaporation can be hindered and the event must be taken into consideration when it comes to modeling the drying of droplets. In order for the crystallization to start and crystals to grow, the solution must to be supersaturated. Supersaturation can be achieved in several ways including changing temperature, evaporation of solvent, chemical reactions and changing solvent composition [18]. In the present system reactions do not occur, and neither is the composition of the solvent changed. When it comes to temperature change, which can be achieved by evaporative cooling of the droplet or heating by the gas, figure 3.1 shows the temperature dependence of NaCl solubility. As can be seen the temperature dependence is low, and crystallization will not be induced by the change of droplet temperature or internal temperature gradients.

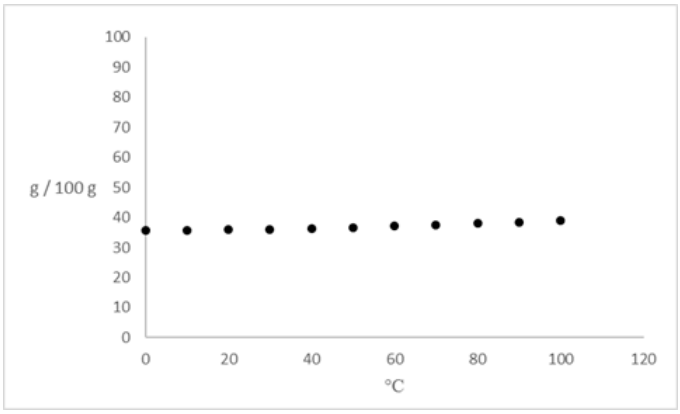

Figure 3.1: Solubility for NaCl as function of temperature [19]

When the droplet dries and the radius is decreasing, there is a possibility of accumulation of solutes or solid particles at the surface of the droplet. If the solid phase is accumulating at the surface a solid shell can be formed during drying. In order to investigate whether the solute diffuses away from the surface faster than the radius decreases, a characteristic time for diffusion was calculated, according to $\tau_{diffusion} = \Delta r^2 / D_{i,m} * 2$ [E]. The characteristic time for diffusion was compared to the time for evaporating all solvent in the droplet, which was obtained from simulations. If the time for diffusion is smaller than the time for evaporation, $\tau_{diffusion} < \tau_{evaporation}$, the species will diffuse away from the surface faster than the radius is decreasing and a shell will not form. Calculations, appended in E, resulted in a normalized characteristic time of diffusion for NaCL to 0.14 compared to the time for evaporation of 1, meaning $\tau_{diffusion} < \tau_{evaporation}$ and thus no shell is forming, and no specific precaution needs to be taken during the simulation of the drying process.

3.3 Parameter study

A reference case was used as starting point for the parameter study, the reference case is presented in appendix A and is based on measurements on a cyclone with a normalized diameter of 1 performed in April 2013. The reference case represents typical operational conditions for the type of cyclone studied.

3.3.1 Significance Study

As described in section 1.1, a typical problem in conventional spray drying is sticking of the discrete phase to the wall, therefore the approach for the parameter study was to investigate drying efficiency until first wall impact. The response variable chosen to represent the drying is mass fraction of water at first wall impact. The first objective with the parameter study was to examine the significance on drying efficiency for different parameters. The parameters to be investigated and their respective interval are presented in table 3.2.

Table 3.2: Parameters and respective interval for the significance study

Parameter	Lower bound (-)	Upper bound (+)
Gas inlet temperature (A)	1	1.5
Drop inlet temperature (B)	0.4	1
Gas inlet velocity (C)	-30% from reference case	+ 30% from ref case
Drop size (D)	0.15	0.6
Cyclone diameter (E)	1	1.4
Drop inlet velocity (F)	0.01	0.09

For the reference case the inlet gas temperature is normalized to 1, and in compliance with the developer of the cyclone-system a realistic temperature increase to be implemented in experiments is 0.5, thereof the upper bound for gas inlet temperature at 1.5. When it comes to droplet temperature, the effect of slight preheating was studied, therefore the upper bound was set to 1. The gas inlet velocity is related to the reference case, and both an increase and decrease of gas inlet velocity were examined. The droplet size distribution is defined in appendix G, and with a normalized volumetric median diameter of 0.4 the effect of having smaller and larger droplets, but still in the range of the spray, was studied. The orthogonal droplet injection velocity was approximated to 0.04 for the actual nozzle, by dividing the volumetric flow rate by the orifice cross sectional area. The velocity was normalized against the maximum velocity in the reference case. The nozzle-to-wall distance in the reference case was 0.18, and the effect of doubling it, resulting in a cyclone diameter of 1.4 was also studied, where the length is normalized against the reference cyclone diameter. The simulations were set up according to design of experiments, and a reduced 2^{6-3} factorial design was used where the main effects are aliased with second and third order effects, in a total of 8 runs. The basic design for the simulation layout is presented in table D.1 in Appendix D. For each factor, or parameter, the effect is calculated according to equation 3.1,

$$Effect_i = \frac{Contrast_i}{N/2} \tag{3.1}$$

where N is the total number of runs, and the contrast is calculated as the sum of the responses, where the sign of each term corresponding to the plus or minus sign in the ith column of D.1 in Appendix D. The sum of square is calculated according equation 3.2,

$$SS_i = \frac{Contrast_i^2}{n2^{k-p}} \tag{3.2}$$

where n is the number of replicates.

The responses from the simulations are presented in table D.2 in Appendix D, and results from the significance study is presented in table 4.5 in section 4.3 under Results.

3.3.2 Enhanced Parameter Study

Based on the results from the significance study, table 4.5, a more detailed parameter study was performed. Since the results showed that the temperature was insignificant for both the gas and droplet they were held constant at a normalized temperature of 1 and 0.4 respectively. The injection velocity was also kept constant at 0.04, representing the actual nozzle. Varying the gas inlet velocity and the nozzle-to-wall distance according to table 3.3, a full 4^2 factorial for gas inlet velocity and nozzle-to-wall distance was performed for in total 4 different droplet sizes. The simulation layout is presented in table D.3 in Appendix D, including responses. Also here the response variable is mass fraction water at wall impact.

Table 3.3: Gas inlet velocity and nozzle-to-wall distance, for detailed parameter study

Parameter	(1)	(2)	(3)	(4)
Nozzle to wall distance	0.18	0.36	0.53	0.71
Inlet gas velocity				
(fraction of reference case)	0.1	0.3	0.5	0.7

4 Result

In this chapter the results from hand calculations and simulations are presented, beginning with the flow field. Further on, discrete phase results and the results from the parameter study are presented.

4.1 Simulations of Flow Field

Generally about the 2D simulations, and specifically in the larger of the two cyclones studied, the velocity components and the static pressure tend to have small oscillations over the iterations. Further on, the mass imbalance was in the order of magnitude of parts per millions, or less, for all simulations considered converged. In subsection 4.1.1, a detailed comparison of the flow field in two and three dimensions is made.

4.1.1 Flow profiles

In order to verify the flow inside the cyclone, velocity components and static pressure was compared between models and between 2D and 3D simulations. The locations of the planes for at which the comparison was made are presented in figure 4.1 below. The pressure and velocities are normalized against the highest number in the reference case.

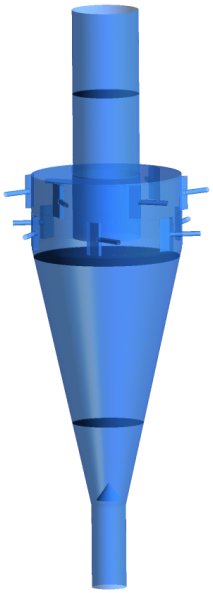

Figure 4.1: Planes at three locations for comparison of flow parameters

In figure 4.2 a comparison is made for different 2D-approaches versus the 3D simulation, at the plane in the upper part of the cone in figure 4.1. As can be seen the axial velocity is over estimated by the 2D model without the zero-swirl zone, by introducing the zero-swirl zone in the vortex finder the profiles are closer to the 3D-profile. Tuning the mass flow rate, even though not perfect, at the inlet in the 2D simulation and the peaks for the axial velocity is close to the 3D simulation. Important to note is that the mass flow rate was not tuned for the 2D simulation without the vortex breaker cross. However, the strongest argument for using the zero-swirl zone is the convergence. For the simulations without the zero swirl zone convergence was hard to achieve, and could as best be seen as a quasi-steady state where both velocities and pressure were oscillating over iterations, and so also the residuals. For the reference case presented in Appendix A, not even the quasi-steady state could be achieved without the zero swirl zone in 2D.

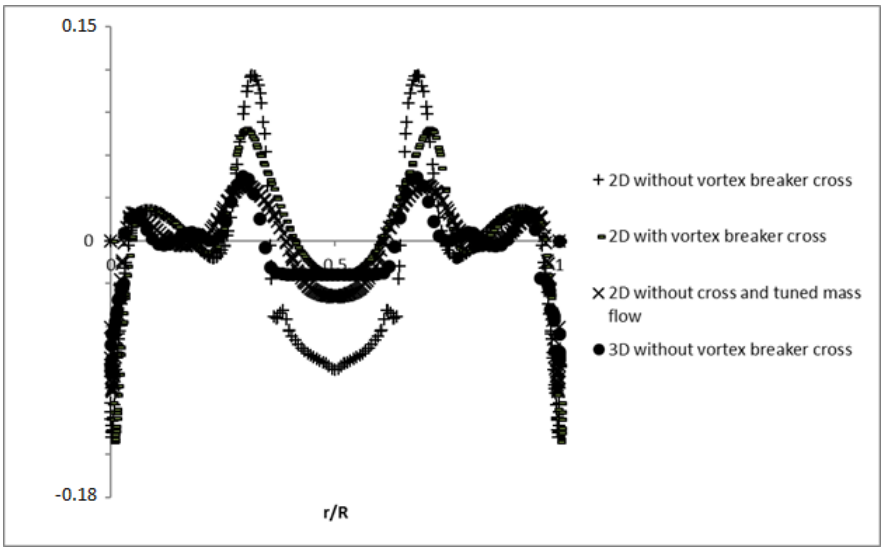

Figure 4.2: Normalized axial velocity profiles, at the middle plane, for different models.

The comparisons in figure 4.3 - 4.5 are between the 2D simulation with the zero-swirl zone and the 3D simulation.

As can be seen in figure 4.3, the conformance between the 2D simulation with the zero swirl zone and the 3D simulation without the vortex breaker cross is low in the vortex finder. In the 3D simulation the air is exiting the cyclone with a swirling motion along the walls in the vortex finder, and gas is entering since the pressure, as a result of the swirling motion, is below atmospheric in the center. The result for the 2D case is that no air is entering through the gas outlet, and the gas velocity has a more even profile over the radius, with a zero swirl component.

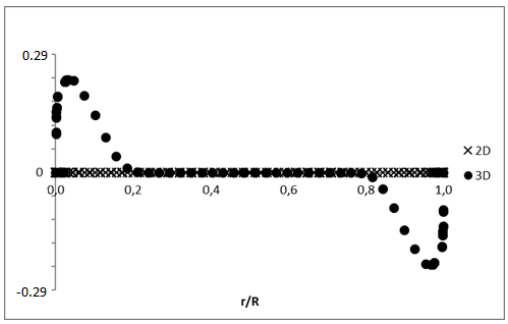

(a) Normalized tangential velocity profile at the upper plane

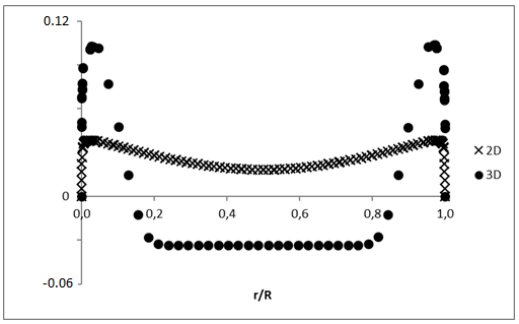

(b) Normalized axial velocity profile at the upper plane

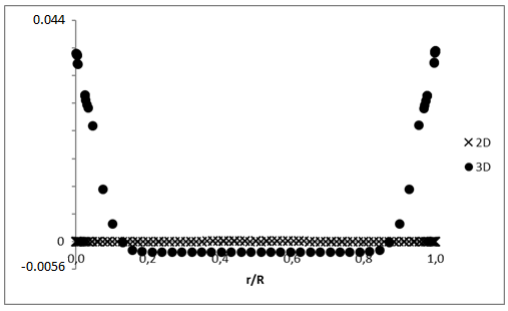

(c) Normalized static pressure at the upper plane

Figure 4.3: Normalized velocity and pressure profile in the vortex finder, at the upper plane of figure 4.1.

Looking at the middle plane, just below the barrel, the conformance is better. In figure 4.4 it can be seen that both the tangential and swirl velocity components is captured better by the 2D simulation than in the vortex finder. The static pressure is underestimated at the walls by the 2D simulation, however, in the center of the cyclone the static pressure is close to the 3D case. Overall the pressure profile is captured by the 2D simulation.

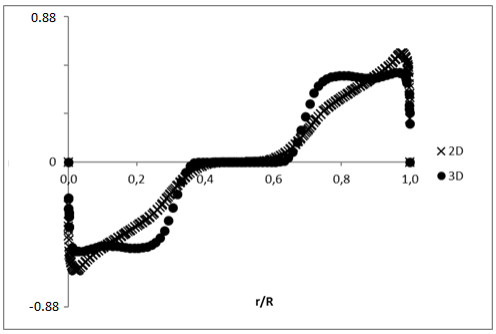

(a) normalized tangential velocity profile at the middle plane

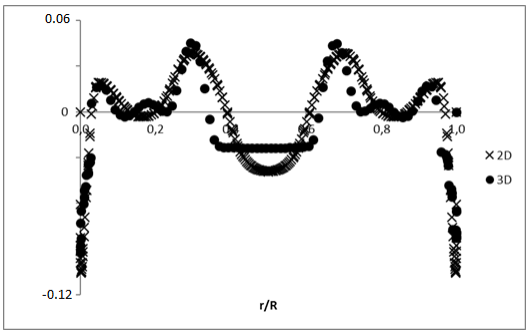

(b) Normalized axial velocity profile at the middle plane

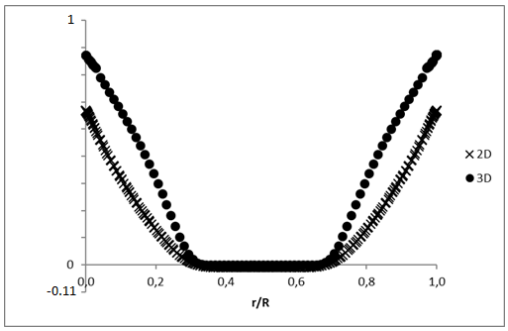

(c) Normalized static pressure at the middle plane

Figure 4.4: Normalized velocity and pressure profile at the plane in the upper part of the cone, middle plane in figure 4.1.

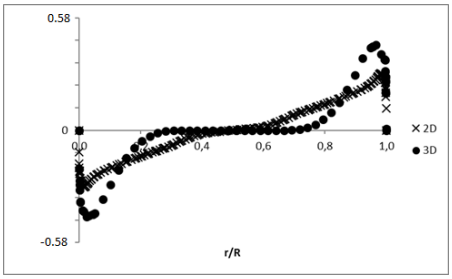

(a) Tangential velocity profile at the lower plane

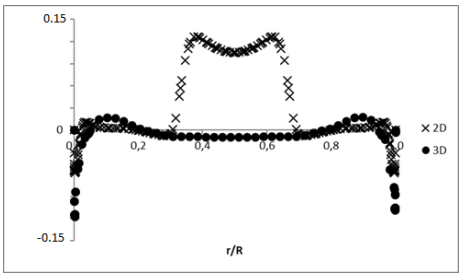

(b) Axial velocity profile at the middle plane

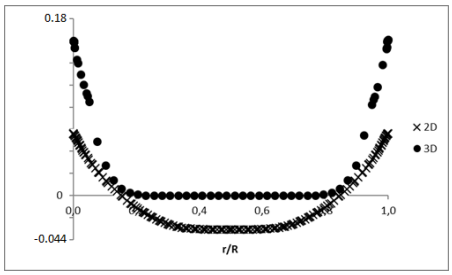

(c) Static pressure at the lower plane

Figure 4.5: Velocity and pressure profiles in the lower part of the cyclone, at the lower plane in figure 4.1

In the lower part of the cyclone, at the lower plane, the profile of the tangential velocity is roughly captured by the 2D model. The axial velocity profile is captured except for the center of the cyclone where the 2D model predict a strong upward motion of the gas in contradiction to the almost zero velocity in the 3D case.

4.2 Discrete Phase Model and Simulations

In this section the results regarding the discrete phase are presented, starting with the properties of the NaCl droplets.

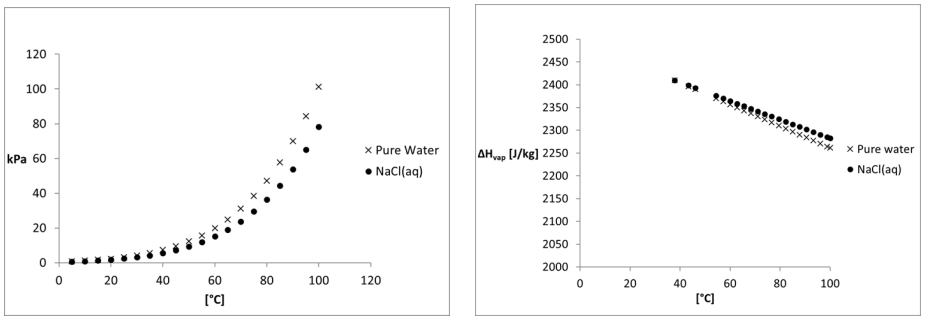

(a) Vapor pressure for sodium chloride solution compared to pure water

(b) Heat of vaporization for water in sodium chloride solution [21] [22]

Figure 4.6: Vapor pressure and heat of vaporization for the droplets.

As can be seen in figure 4.6(a), the vapor pressure for the droplet is lower than for pure water, as expected. When it comes to the heat of vaporization, the temperature dependence is low and a fixed average value was used in the simulations.

Stokes number was calculated for the reference case at different scales. Firstly a large scale where the geometry was the constraint and secondly at the scale for the larger turbulent eddies. The large scale fluid phase normalized velocity is taken to be 0.58, a representative velocity in the region between the nozzle and the wall, for typical operational conditions. Since the droplets are injected almost orthogonal to the velocity field with a comparatively low velocity the dispersed phase velocity is taken to be zero in the calculations, implying that the relative velocity equals the fluid phase velocity.

Given the fluid phase velocity, the drag coefficient was calculated with equation 2.12, the particle response time with equation 2.19 and the characteristic time for the fluid as $\tau_s = l_s/U_s$. The results are presented in table 4.1 and 4.2.

Table 4.1: Stokes number for the large velocity scale, with a fluid phase normalized characteristic time of 0.01

Norm. particle diameter	Norm. particle Reynolds number	Norm. drag Coefficient	Norm. particle response time	Norm. Stokes number
0.15	0.06	0.11	0.035	0.097
0.37	0.15	0.073	0.012	0.375
0.74	0.29	0.71	0.0025	1

Table 4.2: Stokes number for large turbulent eddie scale, with a fluid phase normalized characteristic time of 0.24

Norm. particle diameter	Norm. particle Reynolds number	Norm. drag Coefficient	Norm. particle response time	Norm. Stokes number
0.15	0.0023	1	0.0079	0.01
0.37	0.006	0.48	0.043	0.06
0.74	0.018	0.28	0.14	0.19

Important to note regarding table 4.2 is that the particle is assumed to be in equilibrium with the continuous phase when subjected to the turbulent eddie. Thereof the low particle Reynolds number compared to table 4.1. All numbers are normalized against the highest occurring number, and as previous regarding time and droplet diameter.

4.2.1 Droplet Wall Interaction

The events for a single droplet impinging on the cyclone wall were investigated for the reference case. The Weber number was calculated for droplets of different diameter and corresponding trajectories, the results are displayed in table 4.3.

Table 4.3: Weber number at wall impact

Norm. droplet diameter	Norm. normal Velocity	Norm. angle of impact	Norm. particle Reynolds number	Norm. Weber Number
0.15	0.02	0.5	0.04	0.045
0.37	0.03	0.8	0.22	0.22
0.74	0.03	0.9	0.6	0.56
1	0.04	1	1	1

The results from table 4.3 were used to calculate the events for the impact according to tables 2.1 - 2.2 and are presented in table 4.4 below.

Since the surface roughness of the cyclone walls are not perfectly known, a sensitivity analysis of impact events was performed. Surface roughness from negligible up to the order of magnitude of droplet size does not affect the impact event, neither does the impact angle, which would be the case if the surface roughness is in the order of magnitude of the droplet size.

Applying the same analysis for a case with only 10% of the gas velocity and a nozzle-to-wall distance three times the reference case, and the impact events are in the same region for impact

Table 4.4: Events of impact on the cyclone wall for a single droplet in the reference case

Norm. droplet Diameter	Impact Event dry wall	Impact Event wet wall
0.15	Spread	Splash
0.37	Spread	Splash
0.74	Spread	Splash
1	Spread	Splash

on dry wall. For impact on a wet surface it tends more against a spreading of the droplet instead of splashing.

4.2.2 Comparison Between 2D and 3D Simulations

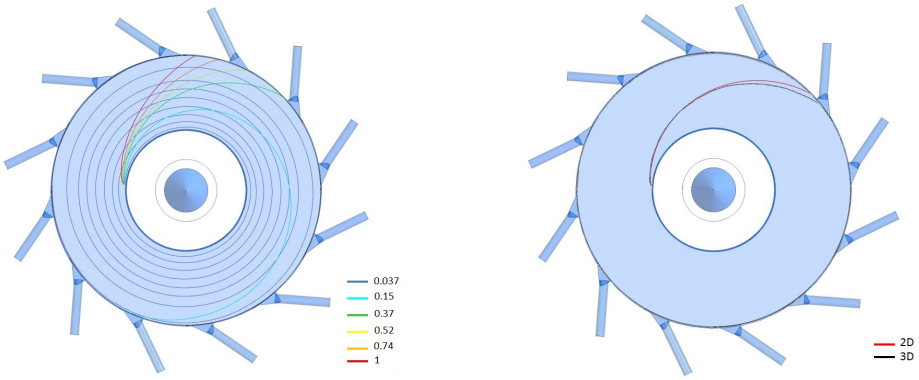

(a) Trajectories for different normalized droplet diameters

(b) Comparison of trajectories for 0.37 droplet between 2D and 3D simulations

Figure 4.7: Droplet trajectories until first wall impact.

The results from figure 4.7(a) and 4.7(b) are in compliance with table 4.1 and 4.2, and it can be seen that the particles are accelerated by the mean flow, but does not follow the flow perfectly, resulting in wall impact. The smaller the particle is, the lower the stokes number is, and the longer it takes until wall impact. As can be seen in figure 4.7(b) the agreement between the 2D and 3D case is good, and the only difference in trajectory can be seen close to the wall. Since the 2D and 3D geometry is the same, same diameter, and the placement of the nozzle also, the trajectory from 2D simulations could be included in the figure of the 3D-trajectory.

4.3 Parameter Study

In table 4.5 below, the results from the significance study are presented. As can be seen, both the temperature of the gas at the inlet and the droplet temperature have negligible influence on the mass fraction of water at first wall impact. Important to note is that the results are valid for the stated intervals only. For the reference case, the time to wall impact is in the order of magnitude of 0.01 seconds, and the heating of the particle for the case with higher gas temperature during this time is negligible. However, lowering the gas velocity, and or the cyclone diameter, the time to wall impact can be increased, resulting in longer time for evaporation. Further on, the most significant parameter is the droplet size. This stems not only from the fact that a smaller droplet has less water to be dried, but also from that the surface area to volume is larger and that a smaller droplet has a lower Stokes number, meaning that it will follow the gas stream better than larger droplets, thus colliding at a later point of time. The drop inlet velocity and cyclone diameter are in the same order of magnitude for the investigated intervals, and the effect of changing the gas inlet velocity contributes less than 3% to the total change. Looking at the sign of the model terms effect estimate, it can be seen whether the term correlates negative or positive to the mass fraction water at wall impact.

Table 4.5: Factor Effects and Sums of Squares for the 2^{6-3} fractional factorial

Model Term	Effect Estimate	Sum of Squares	Percent Contribution
Gas inlet temperature	-0.0175	0,0006125	0.28
Drop inlet temperature	0.002	8×10^{-6}	0.000037
Gas inlet velocity	0.053	0,005618	2.56
Drop size	0.257	0,132098	60.1
Cyclone diameter	-0.145	0,04205	19.1
Drop inlet velocity	0.1405	0,0394805	18.0

4.4 Experiments

The experiments were run with a low loading, in order to be more like the simulations. For the first run a single pressure swirl nozzle of the type presented in appendix G was used. The nozzle was mounted in the vortex finder so that it was aligned with the surface, facing towards the outer wall. Running the experiment with saturated solution and a gas velocity close to the reference case resulted in fouling of the nozzle. The high gas velocity, orthogonal to the injected spray, resulted in destruction of the spray, and larger droplets impacting instantly on the nozzle itself and on the vortex finder. By reducing the gas velocity and placing the nozzle a few centimeters out from the surface of the vortex finder, but still injecting orthogonal to the gas velocity, the destruction of the spray was reduced.

The spray follows the flow in accordance with the simulations. The result from the simulation of

single droplets from the given nozzle was that the smaller droplets in the spray could be dried before the first wall impact, whilst the larger would not, which was confirmed in the experiments.

It was shown during the experiments that particle agglomeration occurred in the cyclone, and that the particle size increased from the dried-droplet size. e.i salt particles at the bottom of the cyclone was significantly larger than the largest droplets in the spray.

Running experiments at different gas velocities showed that a lower gas velocity reduced wall-film build up, which also is in accordance with the simulations. However, even at very low gas velocity the largest particles in the spray will impact on the wall before dried.

When injecting the spray orthogonal to the velocity field the hollow cone spray was disturbed, resulting in larger droplets and thus had an adverse effect on the drying.

Running experiments with a plain orifice nozzle resulted in larger droplets, however, the spray had a higher orthogonal velocity and was less disturbed by the orthogonal flow field, which together with a higher mass flow rate at same operating pressure resulting in heavy wall film buildup.

5 Conclusion and Discussion

The most important conclusion from this thesis is that spray drying is possible in cyclones, however, whether it is feasible compared to traditional spray drying remains to answer. The reason is because only single droplets have been considered, and it could be seen that droplets in the normalized size of 0.22 and smaller could be dried in the studied cyclone before first wall impact. Meaning that spray drying in cyclones is only applicable to a very fine spray.

5.1 Modeling the flow field

As can be seen in the comparison between the 2D and 3D simulations of the flow field, the agreement in the upper part of the cone is good. However, when comparing the 2D simulations with the vortex breaker cross and 3D simulations without the prediction fails in the vortex finder and in the lower part of the cone. The reason why the prediction fails in the vortex finder is because there is nothing breaking the swirling flow in the 3D simulation. The 2D simulation is likely to agree better with 3D simulations with a vortex breaker cross. Because of the reduced swirling flow in the vortex finder for the 2D simulation, no gas is entering through the gas outlet, and the pressure is not as low in the center of the cyclone as for the case without a vortex breaker cross, and therefore gas will enter through the dust outlet for the 3D case and not the 2D case. However, the upper part of the cyclone was described good enough since both 3D and experiments agreed with the 2D simulations, and therefore the results from the parameter study are applicable.

The small oscillations in velocity components and for static pressure could be the result of a PVC, which is not possible to describe with the steady state RNG $k - \mathcal{E}$. And as described in section 2.1, the outcome could be a quasi-steady state with oscillating velocity components.

5.2 Discrete phase

The droplet trajectories from the 2D simulations are very similar to the ones from the 3D simulations until the first wall impact, which was the section of interest. During the experiments it could be seen that the droplets were impacting the wall according to the simulations, and can thus be seen as a validation of the simulations, even though no exact times and trajectories were measured.

During the experiments it could be seen that the smallest droplets in the cyclone was dried before the wall impact, however, a major part of the spray was impacting the wall in the form of droplets. The reason why a larger fraction of the spray impinged the wall than predicted is most probably due to the destructive effect the orthogonal flow field had on the spray.

It was verified in the experiments that the droplets spread against the cyclone wall when impinging, and then traveled along the wall until fully dried. From the salt stripes at the cyclone wall it could also be seen that the total time for evaporation was is the order of magnitude as the time simulated for evaporating all liquid in the largest droplets, and they traveled roughly the same distance as in the simulations.

There was no focus on the separation process in the thesis, however it could be seen that larger particles exited the cyclone through the dust outlet, whilst smaller through the gas outlet. The separation process could not be verified, and in the experiments no particles exited through the dust outlet. A probable reason for this was that a filter was used with a sub-atmospheric pressure at the gas outlet, resulting in a larger inflow through the dust outlet and thus making it harder for particles to exit. However, it was not considered to have any major effect on the flow field in the barrel, where the studied spray was injected.

A possible problem with the small droplets is that the probability for them to leave the cyclone through the gas outlet is high, which is not wanted. However, the observation of agglomeration of particles in the cyclone could be a solution to this problem. It was also seen that the particles stayed close to the wall, as predicted in the simulations of the discrete phase, so they will most likely not collide with any wet particles if those are dried well before reaching the wall.

The modeled heat and mass transfer could be validated in a very quantitative manner, since the drying occurred as simulated as far as could be observed. Further on, since internal temperature gradients has negligible effect on whether the crystallization starts on the surface or not, the assumption of homogeneous droplet temperature, as used in equation 2.30, has no effect on the crystallization process.

5.3 Parameter study

The results as far as could be seen during the experiments agreed, and the predicted behavior was verified. The effect of gas velocity on Stokes number could be seen, and also roughly the overall drying efficiency and higher gas velocity led to more sticking of the particles to the wall.

The combination of a large diameter and low gas velocity is most feasible and both the simulations and experiments shows that the smaller droplets from the nozzle presented in appendix G can be dried before wall impact.

6 Future Work

According to the simulations, the actual nozzle is giving to large droplets, in comparison to what could be dried before impinging the wall. This was also confirmed during the experiments. Adding to the large droplet the clogging of the pressure swirl nozzle, other alternatives such as two phase nozzles with smaller droplets should be investigated. Further on, due to the destruction of the spray, different injection angles and type of sprays should be considered. The hollow cone spray may not be the best suited.

An interesting observation from the experiments was the agglomeration of particles. The agglomeration resulted in larger particles exiting the cyclone than the largest droplets in the spray. With that in mind in addition to a nozzle producing a very fine spray, it might be possible to dry the small droplets and when they approach and collide with the wall agglomerate them into a size that can exit through the dust outlet. However, if there is a large or small fraction of the particles that can reach a critical mass for exiting through the dust outlet is not known.

Since neither collision of droplets nor breakup and high loadings were simulated, future work could include these features. The effects of changing the angle of the gas inlets, and adding more nozzles, e.g. So the inlet gas streams overlaps, could also be investigated.

Bibliography

[1] Bengt Andersson, Ronnie Andersson, Love Håkansson, Mikael Mortensen, Rahman Sudiyo and Berend van Wachem, 9th edition of Internal Chalmers version of "Computational Fluid Dynamics for engineers", Göteborg march 2013.

[2] *"An Investigation of Particle Trajectories in Two-Phase Systems"*. J.Fluid Mech.. 55(2). 193-208. September 26 1972.

[3] ANSYS FLUENT Theory Guide, Release 14.0, November 2011

[4] R. B. MacMullin, Algorithms for the Vapor Pressure of Water Over Aqueous Solutions of Salt and Caustic Soda, R. B. MacMullin Associates, Niagara Falls, New York

[5] Yoon, S. S. and DesJardin, P. E., Modeling Spray Impingement using Linear Stability Theories for Shattering Droplets, 2006, International Journal for Numerical Methods in Fluids, Vol. 50, pp. 469-489.

[6] Cossalie, G. E., Coghe, A. and Marengo, M., The Impact of a Single Drop on a Wetted Solid Surface, Experiments in Fluids, Vol. 22, pp. 463 ≈ 472.

[7] Stanton, D. W. and Rutland, C. J., Modeling Fuel Film Formation and Wall Interaction in Diesel Engines, SAE960628, 1996.

[8] Bai, C. X., Ruche, H. and Gosman, A. D., 2002,Modeling of Gasoline Spray Impingement, Atomization and Sprays, Vol. 12, pp. 1 ≈27

[9] Yarin, S. H. and Weiss, D., 1995, Impact of Drops on Solid Surface: Self-Similiar Capillary Waves and Splashing as a New Type of Kinematic Discontinuity, Journal of Fluid Mechaniocs, Vol. 283, pp. 141 ≈ 173.

[10] J.R. Welty, C. E. Wicks, R. E. Wilson., G. L. Rorrer., Fundamentals of Momentum, Heat and Mass Transfer, USA, wiley.

[11] A.J. Hoekstra, J.J. Derksen, H.E.A. Van Den Akker, An experimental and numerical study of turbulent swirling flow in gas cyclones, Chem. Eng. Sci. 54 (1999) 2055–2065.

[12] A.J., Hoekstra, 2000, Gas Flow Field and Collection Efficiency of Cyclone Separators,

[13] Yakhot, V., Orszag, S.A., Thangam, S., Gatski, T.B. and Speziale, C.G. (1992), "Development of turbulence models for shear flows by a double expansion technique", Physics of Fluids A, Vol. 4, No. 7, pp1510-1520.

[14] H.F. Meier, M. Mori, Anisotropic behavior of the Reynolds stress in gas and gas-solid flows in cyclones, Powder Technol. 101 (1999) 108-119.

[15] A.J. Hoekstra, J.J. Derksen, H.E.A. Van Den Akker, An experimental and numerical study of turbulent swirling flow in gas cyclones, Chem. Eng. Sci. 54 (1999) 2055–2065.

[16] G. Gronald, J.J. Derksen, Simulating turbulent swirling flow in a gas cyclone: A comparison of various modeling approaches, Powder Technology, Volume 205, Issues 1–3, 10 January 2011, Pages 160-171, ISSN 0032-5910 (http://www.sciencedirect.com/science/article/pii/S0032591010004821)

[17] ANSYS Fluent User Guide, Release 14.0, November 2011

[18] J. D. Seader, J. Henley, Separation Process and Principles, Second Edition, Wiley, 2006

[19] IUPAC-NIST Solubility Database, Version 1.0 NIST Standard Reference Database 106, IUPAC 2007-12-6.

[20] Bai, C. X. and Gosman, A. D., 1995, "Development of Methodology for Spray Impingement Simulation," SAE 950283

[21] Measurement of thermodynamic properties of saline solutions, David knoeb et al, Oklahoma state University, 1968

[22] Army Corps of Engineers' water quality model CE-QUAL-R1, Environmental Laboratory, 1982

[23] N. Fröessling, Gerlands Beitr. Geophys., 52, 170 (1939)

[24] S.Evnochides and G. Thodos, A.I.Ch.E J., 5, 178 (1960)

[25] W. Ranz and W. Marshall, chem. Engr. Progr. 48, 141 (1952)

[26] E. Stendal, Multiphase Flows in Cyclone Separators, Göteborg 2013

A Reference Case

The reference case is based on measurements performed by Elkem on a cyclone with a normalized diameter of 1, this normalization is used for the length scale in the report together with the normalization against the inlet tangential velocity. However, with all nozzles in use, in contrast to some of the simulations. The measured volumetric flow rate was recalculated to a velocity for the 2D simulations, and a measured pressure was used for inlet conditions for the 3D simulations.

Table A.1: Settings and boundary conditions for the reference case in 2D

Parameter	Value
Normalized inlet radial velocity	-0.0077
Normalized inlet tangential velocity	1
Normalized inlet temperature	1

B Droplet Curvature Effect on Vapor Pressure

Below is a approximation of how large the effect the droplet curvature has on the vapor pressure at 300 K. From the Kelvin equation the difference in vapor pressure can be expressed as

$$\frac{P}{P_0} = exp(\frac{2\gamma V_m}{rRT}) \tag{B.1}$$

Inserting the values:

$$\gamma = 0.9836 \times \gamma_{20^\circ C} = 0.9836 \times 82e-3 = 0.0807\ [N/m]$$
$$R = 8.314\ [J/Kmol]$$
$$T = 300\ [K]$$
$$r = 25e-6\ [m]$$

and the molar volume, V_m, from the fact that a saturated solution of NaCl has the density of 1200 kg/m3 and molarity of 6.125 mol/L

$$Vm = \frac{x_{NaCl}M_{NaCl} + x_{H2O}M_{H2O}}{\rho_{mixture}} = \frac{6.125 + 5.86}{1200} = 0.010\ [m^3/mol] \tag{B.2}$$

which gives

$$\frac{P}{P_0} = exp(\frac{2\gamma V_m}{rRT}) = exp(\frac{2 \times 0.087 \times 0.01}{25e-6 \times 8.314 \times 300}) = 1.028 \tag{B.3}$$

C Estimating Distance to first Grid Point

First the reynolds number was calculated:

$$Re = \frac{\rho U_{freestream} L_{characteristic}}{\mu} \tag{C.1}$$

Then the *Schlichting skin-friction correlation* was used for calculating the skin friction factor

$$C_f = [2log_{10}(Re) - 0.65]^{-2.3} \tag{C.2}$$

The wall shear stress is then computed:

$$\tau_w = C_f * \frac{1}{2} \rho U^2_{freestream} \tag{C.3}$$

then a characteristic velocity scale, friction velocity, is defined and calculated according to equation C.4

$$u_* = \sqrt{\frac{\tau_w}{\rho}} \tag{C.4}$$

finally the wall distance can be estimated as

$$y = \frac{y^+ \mu}{\rho u_*} \tag{C.5}$$

The density and viscosity were taken for air at approximate process conditions.

Reference

Schlichting, Hermann (1979), Boundary Layer Theory, ISBN 0-07-055334-3, 7th Edition

D factorial

Table D.1: 2^{6-3} Simulations layout, basic design

Run	A	B	C	D=AB	E = AC	F=BC	
1	-	-	-	+	+	+	def
2	+	-	-	-	-	+	af
3	-	+	-	-	+	-	be
4	+	+	-	+	-	-	abd
5	-	-	+	+	-	-	cd
6	+	-	+	-	+	-	ace
7	-	+	+	-	-	+	bcf
8	+	+	+	+	+	+	abcdef

Table D.2: Response from reduced factorial design

Treatment	Response (mass fraction water at wall impact)	norm. time to wall impact
def	0.717	0.13
af	0.536	0.10
be	0.270	0.26
adb	0.706	0.11
cd	0.723	0.057
ace	0.355	0.099
bcf	0.660	0.046
abcdef	0.703	0.072

Table D.3: $4^2 factorial$

Run	Diameter (A)	Velocity (B)	Response diameter: 0.37	Response diam: 0.67	Response diam: 1	"barely dried" diam: 0.52
1	(1)	(1)	0.66894	0.71685	0.72615	0.705862
2	(2)	(1)	0.46752	0.69464	0.71939	0.66001
3	(3)	(1)	0	0.65979	0.71198	0.55014
4	(4)	(1)	0.0000	0.57628	0.70105	0.014056
5	(1)	(2)	0.69668	0.71955	0.72578	0.713449
6	(2)	(2)	0.67217	0.71238	0.72243	0.701574
7	(3)	(2)	0.60508	0.70061	0.71845	0.679026
8	(4)	(2)	0.0000	0.66494	0.71031	0.58488
9	(1)	(3)	0.71162	0.72264	0.72635	0.71945
10	(2)	(3)	0.69273	0.71670	0.72370	0.709679
11	(3)	(3)	0.65836	0.70830	0.720564	0.695662
12	(4)	(3)	0.59835	0.69772	0.71669	0.67596
13	(1)	(4)	0.715013	0.723603	0.72672	0.7209146
14	(2)	(4)	0.701239	0.71886	0.7245	0.7136172
15	(3)	(4)	0.68443	0.717559	0.72626	0.7084591
16	(4)	(4)	0.641484	0.70407	0.71848	0.6879704

E Characteristic Time for Diffusion

Loose random packing of mono-sized spheres gives approximately 40% void fraction.[F.A.L. Dullien, "Porous Media. Fluid Transport and Pore Structure", 2nd edition, Academic Press Inc., 1992] However the salt crystals (cubic) will neither be spheric nor mono-sized, however, a void fraction of 40% can be used as approximation.

Given the density of the crystalline NaCl, $\rho_{NaCl} = 2170$ kg/m^3, the remaining particle after water evaporation can be estimated. Having a initial droplet radius of $25\mu m$ with a mass fraction of 27%, corresponding to saturated solution at operating conditions, and density of 1200 kg/m^3 the remaining particle mass (dry) will be 2.12e-11 kg. With a crystal density of 2170 kg/m3 and void fraction of 40% this gives a radius of $16\mu m$. Meaning that the droplet radius decreases from 25 to $16\mu m$ during drying.

An important question to answer is whether the characteristic time of evaporation is faster or slower than that of the diffusion for NaCl in the droplet. In the former case the crystals will start to form at the surface of the droplet, and in the latter inside the droplet.

How long time does is take for sodium chloride to diffuse 25-$16\mu m$?

From table E.1 the diffusivity of sodium chloride at 291 K is 1.54e-9 m$^2/s$, the time taken for the diffusive transport can be approximated as

$$t = distance^2/Diffusivity * 2 = (9e-6)^2/(2 \times 1.54e-9) = 0.026s$$

at process conditions the diffusivity can be approximated as [Fundamentals of Momentum, Heat and Mass Transfer, J.R. Welty, C.E. Wicks., R.E. Wilson., G.L. Rorrer., Wiley 2008, USA]

$$D_{ABT_2} = \frac{D_{ABT_1}}{(\frac{T_c - T_2}{T_c - T_1})^n} = \frac{1.54e-9}{(\frac{647-323}{647-291})^6} = 2.71e-9$$

And the time calculated to

$$t = (9e-6)^2/(2 * 2.71e-9) = 0.015s$$

Table E.1: Binary mass diffusivity of Sodium Chloride in water [R. E Treybal, Mass Transfer Operations, McGraw-Hill, New York, 1955, p. 25]

Specie	Temperature K	Concentration kmol/m^3	Diffusivity m^2/s
Sodium Chloride	291	5.4	1.54e-9

F User Defined Function - Multicomponent Droplet Vapor Pressure

```
/************************************************************************
UDF for defining the vapor particle equilibrium
for multicomponent particles
************************************************************************/

# include "udf.h"

DEFINE_DPM_VP_EQUILIB(nacl_vpe,p,cvap_surf,Z)
{
                int is;
                real molwt[MAX_SPE_EQNS];
                real M = 6.1;                                                   /* saturation
molality nacl solution */
                Thread *t0 = P_CELL_THREAD(p);                                  /* cell thread of particle location
*/
                Material *gas_mix = THREAD_MATERIAL(t0);          /* gas mixture material */
                Material *cond_mix = P_MATERIAL(p);                             /* particle mixture material */
                int nc = TP_N_COMPONENTS(p);                                    /* number of particle components */
                real Tp = P_T(p);                                               /* particle
temperature */
                real molwt_cond = 0.;                                           /* reciprocal
molecular weight of the particle */
                for (is = 0; is < nc; is++)
                   {
                                int gas_index = TP_COMPONENT_INDEX_I(p,is); /* index of vaporizing component in the gas
phase */


                                if (gas_index >= 0)
                                   {
                                                /* the molecular weight of particle material */

                                   molwt[gas_index]=MATERIAL_PROP(MIXTURE_COMPONENT(gas_mix,gas_index),PROP_mwi);
                                   molwt_cond += TP_COMPONENT_I(p,is) / molwt[gas_index];
                                   }
                   }

                /* prevent division by zero */
                molwt_cond = MAX(molwt_cond,DPM_SMALL);
                for (is = 0; is < nc; is++) {

                /* gas species index of vaporization */
                int gas_index = TP_COMPONENT_INDEX_I(p,is);
                if( gas_index >= 0 )
                   {

                   /* condensed material */
                   Material * cond_c = MIXTURE_COMPONENT( cond_mix, is );

                   if(TP_COMPONENT_I(p,is)/(molwt[gas_index]*molwt_cond)>0.001)
                   {

                   real p_saturation = DPM_vapor_pressure(p, cond_c, Tp);   /* saturation pressure for pure water [Pa],
antoine */

                        if (p_saturation < 0.0)
                         p_saturation = 0.0;

                      /* vapor pressure over the surface, nacl solution */
                      cvap_surf[is] =p_saturation*(1.0-((M-3.0)*(0.0019772-0.00001193*(Tp-
273.15))+0.035)*M)/UNIVERSAL_GAS_CONSTANT / Tp;
                                /* UNIVERSAL_GAS_CONSTANT =[8314.34 J/Kmol-K] */

                  }
                }
                }

                /* compressibility for ideal gas */
                *Z = 1.0;

}
```

Figure F.1: UDF for defining vapor pressure for multicomponent droplets in ANSYS Fluent

G Nozzle

The nozzle produces a hollow cone with a normalized spray angle of approximately 1, with heavy concentration of the liquid in a ring, as described in figure G.1.

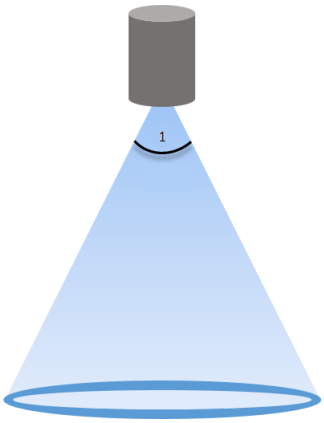

Figure G.1: Pressure swirl nozzle of the type used in the experiments.

In figure G.2 the normalized distribution of droplet sizes is displayed, and as can be seen the range of droplet covers 0 - 1 in size, which is the reference for droplet diameter normalization, with a volumetric normalized median diameter of 0.37.

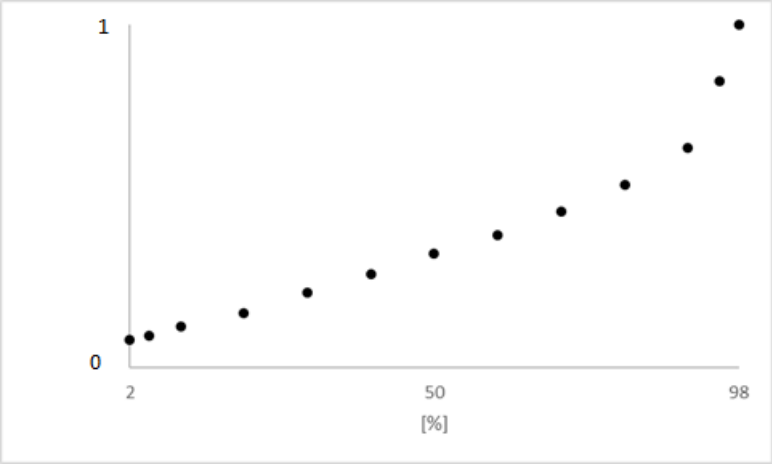

Figure G.2: Droplet diameter vs. accumulated volume percentage.

[Data Sheet No. 12135-194M, Spraying Systems Co. North Avenue a Schmale Rd. P.O Box 7900 Wheaton, 1995-11-27]